Chin. Geogra. Sci. 2019 Vol. 29 No. 5 pp. 798–808
https://doi.org/10.1007/s11769-019-1050-2

Springer Science Press
www.springerlink.com/content/1002-0063

Impact of the Zhalong Wetland on Neighboring Land Surface Temperature Based on Remote Sensing and GIS

DU Jia[1], SONG Kaishan[1], YAN Baohua[2]

(1. *Northeast Institute of Geography and Agroecology*, *Chinese Academy of Sciences*, *Changchun* 130102, *China*; 2. *Jilin Natural Resources Investigation and Planning Center Co*., *Ltd*, *Changchun* 130061, *China*)

Abstract: Wetlands play a key role in regulating local climate as well as reducing impacts caused by climate change. Rapid observations of the land surface temperature (LST) are, therefore, valuable for studying the dynamics of wetland systems. With the development of thermal remote sensing technology, LST retrieval with satellite images is a practicable way to detect a wetland and its neighboring area's thermal environment from a non-point visual angle rather than the traditional detection from a point visual angle. The mono-windows (MW) method of retrieving LST was validated. On the basis of estimated LST, we used Geographical Information System (GIS) technology to study the impact of wetland reclamation on local temperatures at a regional scale. Following that, correlations between LST and the wetland were analyzed. The results show that: 1) It is feasible to retrieve the LST from Landsat 8 OLI satellite images with MW model. The model was validated with the land surface temperature observed in four meteorological stations when the satellite scanned the study region. The satellite retrieval error was approximately 1.01°C. 2) The relationship between the spatial distribution of land surface temperatures and the Zhalong wetland was analyzed based on GIS technology. The results show that wetland has an obvious influence on LST, and that this influence decreases with increasing distance from the wetland. When the distance from the wetland was less than 500 m, its influence on LST was significant. Results also illustrated that the effect of the wetland's different land use/land cover's LST distribution varied with different seasons.

Keywords: land surface temperature; cold-humid effect; influence distance; Zhalong wetland

Citation: DU Jia, SONG Kaishan, YAN Baohua, 2019. Impact of Zhalong Wetland on Neighboring Land Surface Temperature Based on Remote Sensing and GIS. *Chinese Geographical Science*, 29(5): 798–808. https://doi.org/10.1007/s11769-019-1050-2

1 Introduction

Wetlands have been called 'the kidneys of the earth'. They have a total global area of more than 12.8 million km^2 and are considered to be one of the largest ecosystems in the world, along with forests and oceans (An, 2004). They have very high biodiversity and numerous ecological roles, including supply, regulation, support and cultural functions (MEAB, 2005). Wetland changes have impacted on climate at different spatial scales (Dickenson, 1991; Hostetler, 1991; Pitman, 1991; Hostetler et al., 1993; Gorham, 1995; Lofgren, 1997; Chen, 1999). At large and mesoscales, wetlands influence global and regional climate change because their carbon emissions and storage are important contributory factors for the global carbon cycle, and thus greenhouse gases in the atmosphere (Song, 2003; Tong and Zeng, 2006; Hu et al., 2009; Yang and Tong, 2011). At a smaller scale, wetlands play an important role in determining local climates, primarily through the cold-humid effect (Gao et al., 2002; Gao et al., 2003; Krinner, 2003; Nie and Wang, 2010). When compared to other land-use types, wetlands show large differences in albedo, heat capacity, roughness and energy exchange. This means

Received date: 2018-03-30; accepted date: 2018-07-26
Foundation item: Under the auspices of National Key Research and Development Program of China (No. 2016YFA0602301-1), Strategic Planning Project of Northeast Institute of Geography and Agroecology (IGA), Chinese Academy of Sciences (No. Y6H2091001)
Corresponding Author: DU Jia. E-mail: jiaqidu@iga.ac.cn

that they can locally reduce temperature and raise humidity under conditions of cold radiation and evapotranspiration (Bonan, 1995; Gong et al., 2011). Several previous studies concentrated on the cold-humid effect of wetlands producing broader scale environmental change. Working in the Sanjiang Plain of northeast China, Gao et al. (2002) found that temperatures measured in wetlands, both daytime and night time, were always higher than those from the surrounding farmland. Saaroni and Ziv (2003) carried out observations around a pond in a Mediterranean urban park and found lower temperatures, higher relative humidity and lower heat stress indexes downwind of the pond, compared with those from stations located upwind. Li et al. (2007) used a numerical simulation method to estimate the temperature decrease and humidity-changing effects of wetlands on the surrounding areas. They developed a model of air flow and diffusion combined with the dynamic moisture characteristics.

In previous studies, research into the cold-humid effects of wetland has been based mostly on small scale field observation, and research at a regional scale is rare. Field observation can not provide the synchronized, quantitative large scale information which would be necessary for discussion of the range, amplitude and impact factors of a large wetland's cold-humid effect, but remote sensing can. Many studies have used remote sensing to extract thermal environmental features and analyze their temporal or spatial distribution. Thermal information is mainly gained by the retrieval of land-surface temperature (LST). Because of the different characteristics of thermal sensors, LST retrieval methods have developed in tandem with them. The Advanced Very High-Resolution Radiometer (AVHRR), the Moderate-Resolution Imaging Spectroradiometer (MODIS), the Advanced Spaceborne Thermal Emission and Reflection Radiometer (ASTER) and other multi-channel thermal satellite images allow the application of a split-window method (Price, 1983; Prata, 1994; Sobrino et al., 1996) and temperature/emissivity separation (TES) (Gillespie et al., 1998). Images from Landsat-5 TM, Landsat-7 ETM+ and other satellites with only one thermal channel allow the use of the single-window inversion method with either Qin et al. (2001)'s algorithm or Jiménez-Muñoz and Sobrino's (2003) algorithm. A great deal of research has been directed towards the close relationship between LST and surface features. Stable triangle (Price, 1983; Carlson et al., 1995; Gillies and Carlson, 1995) and relationships between LST and NDVI (Normalized Difference Vegetation Index) have been extensively reported (Han et al., 2005; Chen et al., 2006).

The Zhalong wetland is one of the major wetlands of China, and is located on the Songnen Plain of Songhua River Basin in Heilongjiang Province. In 1992, the Zhalong wetland was listed as a Wetland of International Importance. It is home to about 265 different types of bird including large wading and swimming species. Most belong to the Palearctic species and a few are Oriental. Unfortunately, some very rare species, such as the white-naped and red-crowned cranes, are now on the edge of extinction in this area because of the shrinking of the wetland itself. During the past two decades, a warmer and drier regional climate, together with disturbance from intensive, uncontrolled human activities, have caused degradation and shrinkage of the wetland, and the environment of Zhalong has become more vulnerable (Han et al., 2007; Huang et al., 2007; Yuan et al., 2009). It is necessary to study the wetland's effect on local climate in this region in order to lay the foundation for a future study of the impact of wetland change. In this paper, thermal environmental features were retrieved with Landsat8 OLI imaging. Analyses of the patterns as influenced by the Zhalong wetland were carried out and the mono-windows method of retrieving LST was validated. On the basis of estimated LST, we have tried to study the impact of wetland reclamation on local temperatures at a regional scale using geographic information system (GIS) technology. This both helps to enrich the case study of environmental effects from wetland changes, whilst at the same time, contributing significantly to a quantitative understanding of wetlands' ecological functioning.

2 Study Area and Data

2.1 Study site

The Zhalong wetland reserve occupies around 2100 km^2, and lies between 46°52′N to 47°32′N latitude and 123°47′E to 124°37′E longitude (Fig. 1). The average altitude of the wetland region is 144.0 m, and it is in a temperate continental monsoon climatic zone. The mean annual temperature is about 3.9°C and the annual precipitation is approximately 402.7 mm. Marsh, lake and

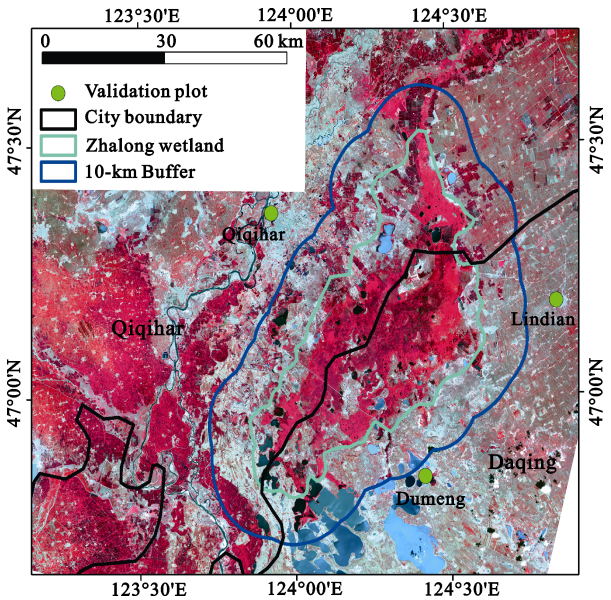

Fig. 1 Location of Zhalong wetland, Heilongjiang Province, China

paddy fields are the main land cover types in the natural reserve (Wang et al., 2006). Reed marshes comprise the main part of the central region and dense reeds cover 80%–90% of the wetland's ground surface. Emergent and shoreline plants such as common reed and *Typha* are the main components of the ecosystem within the wetland, while the peripheral farmland is mainly composed of maize (Cui, 2002; Tong et al., 2008; Wang et al., 2009; Wo and Sun, 2010). These wetlands are important to the well-being of a number of wildlife species, especially endangered cranes (e.g., *Grus japonensis* and *Grus vipio*) and wading species (e.g., *Ardea cinerea*) (Li et al., 1998; 1999; Qiu et al., 2005). For conservation management, the Zhalong wetland is divided into a central zone, a buffer zone and an experimental zone based on their ecological and environmental functionalities.

2.2 Data sets

Landsat 8 Operational Land Imager (OLI)/Thermal Infrared Sensor (TIRS) images were selected for their improved signal-to-noise performance over Thematic Mapper (TM) and Enhanced Thematic Mapper Plus (ETM+) images. All Landsat images used were at the L2 level. The U.S. Geological Survey (USGS) offers on-demand production of Landsat 8 Operational Land Imager/Thermal Infrared Sensor (OLI/TIRS) Surface Reflectance data through EarthExplorer (https://earthexplorer.usgs.gov/). Surface Reflectance products provide an estimate of the surface spectral reflectance as it would be measured at ground level in the absence of atmospheric scattering or absorption. The Surface Reflectance products are generated at the Earth Resources Observation and Science (EROS) Center at a 30 m spatial resolution. The EROS Science Processing Architecture (ESPA) interface corrects satellite images for atmospheric effects to create Level-2 data products. Landsat 8 Surface Reflectance data are generated from the Landsat Surface Reflectance Code (LaSRC). LaSRC makes use of the coastal aerosol band to perform aerosol inversion tests, uses auxiliary climate data from MODIS and uses a unique radiative transfer model. Additionally, LaSRC hardcodes the view zenith angle to '0', and the solar zenith and view zenith angles are used for calculations as part of the atmospheric correction. Details about LaSRC and Landsat 8 Surface Reflectance data products can be found in the Landsat 8 Surface Reflectance Product Guide. Descriptions of the Landsat 8 images used in this study are presented in Table 1.

Four meteorological sites operated by the China Meteorological Administration (CMA) were selected for LST validation, corresponding to 6 scenes of Landsat 8 imagery (Fig. 1; Table 1). The meteorological sites were Qiqihaer (abbreviated as QQHE), Dumeng (DM), Fuyu (FY) and Lindian (LD), which can provide hourly ground meteorological data, such as land surface temperature, air pressure, relative humidity and wind speed.

3 Methods

3.1 Classification of land use/land cover

Improved and up-to-date land use/land cover (LULC) data sets that classify land use practices over extensive LULC areas in the Zhalong wetland are needed to enable a comprehensive analysis. A combination of an

Table 1 Description of Landsat Operational Land Imager (OLI)/Thermal Infrared Sensor (TIRS) scenes used in this paper

Acquisition date	2017-04-16	2017-05-02	2017-06-19	2017-07-05	2016-09-20	2017-10-25
Cloud cover (%)	0.09	5.39	5.24	0.23	0.01	0.03
Season	Spring	Spring	Summer	Summer	Fall	Fall

unsupervised iterative self-organizing data analysis technique (ISODATA) and a hierarchical decision tree classification were employed using the six-month time-series of Landsat NDVI data filtered with the Savitzky-Golay algorithm (Savitzky and Golay, 1964). Savitzky and Golay (1964) proposed a simplified least squares-fit convolution for smoothing and computing derivatives of a set of consecutive values (a spectrum). The convolution can be understood as a weighted moving average filter with weighting given as a polynomial of a certain degree. The weight coefficients, when applied to a signal, perform a polynomial least-squares fit within the filter window (Chen et al., 2004). This polynomial is designed to preserve higher moments within the data and to reduce the bias introduced by the filter. All the filtering was implemented in Interactive Data Language (IDL), and then the filtered NDVI time-series data were imported back to ENVI 4.3 for regional LULC classification. According to the Chinese national LULC classification scheme, and the situation in the study area, our land cover classification scheme using Landsat8-NDVI-30m data, includes forest, marsh, saline-alkali land, resident, grassland, water body and two classes of croplands (paddy field and dry farmland). An unsupervised classification procedure (ISODATA) was used for image classification (ENVI 4.3), because it enables the identification of all the important spectral groupings without the need to initially determine which are thematically significant. Finally, up to 50 training and validation samples for each of the six classes were extracted from a GF-1A scene acquired on July 17, 2017. They were checked with 100 field samples collected during the summer season of that year.

3.2 Theoretical basis of the MW algorithm for Landsat 8 data

The Landsat 8 thermal infrared (TIR) instrument designed with two TIR bands is very suitable for the split-window algorithm for LST retrieval. Recently, Rosenstein et al. (2014) adapted the two-factor split-window algorithm of Qin et al. (2001) for Landsat 8 Thermal Infrared Sensor (TIRS) data. Jiménez-Muñoz et al. (2014) also adapted their single-channel (SC) algorithms and split-window algorithms to Landsat 8 TIRS data for LST retrieval. However, several artifacts, including banding and absolute calibration discrepancies that violate the requirements in some scenes (Montanaro et al., 2014), had been observed in the TIRS data. The United States Geological Survey (USGS) issued a notice on its websites relating to the calibration of Landsat 8 TIRS thermal bands (United States Geological Survey, 2014). Prior to the early-2014 update, users might subtract 0.29 W/(m^2·sr·μm) from every TIRS Band 10 calibrated radiance value and 0.51 W/(m^2·sr·μm) for every TIRS Band 11 calibrated radiance value to provide values closer (on average) to the actual radiances. The root mean square (RMS) variability in the required adjustment was roughly 0.12 W/(m^2·sr·μm) (0.8 K) for Band 10 and 0.2 W/(m^2·sr·μm) (1.75 K) for Band 11 (Price, 1983; Barsi et al., 2014). Therefore, it is still necessary to develop a practical algorithm with detailed determination of the required parameters for LST retrieval from the single Landsat 8 TIRS Band 10 data.

The theoretical basis of thermal remote sensing is that the thermal radiance observed by the remote sensor is mainly from the ground emittance, which, according to the blackbody theorem of radiance, can be determined as a function of temperature at a specific wavelength, i.e., the thermal range of the spectrum (Sobrino et al., 1991). Assuming the land surface as Lambertian, Qin et al. (2001) developed a mono-window algorithm for LST retrieval from Landsat 5 TM data, which only has one thermal band (Band 6). Derivation of the algorithm was composed of several reasonable assumptions and approximations used to estimate LST. The upwelling and downwelling atmospheric emittances were computed as an integrative function of atmospheric emittance (expressed as the Planck radiance function with profile air temperature) at various altitudes and approximated through mean atmospheric emittance with an effective mean atmospheric temperature (T_a). Moreover, Planck's radiance function was linearized through Taylor expansion to approximate the radiance of the ground by the received radiance.

Though Landsat 8 TIRS has two thermal bands (10 and 11), only data from Band 10 are suitable at the moment for LST retrieva1 due to the larger uncertainty in the Band 11 values (Barsi et al., 2014; Montanaro et al., 2014; United States Geological Survey, 2014). Therefore, we used the mono-window algorithm in the following form for LST retrieval from the Landsat 8 TIRS Band 10 data:

$$T_s = [a_{10}(1 - C_{10} - D_{10}) + (b_{10}(1 - C_{10} - D_{10}) + C_{10} + D_{10})T_{10} - D_{10}T_a]/C_{10} \quad (1)$$

where T_s is the LST retrieved from the Landsat 8 TIRS Band 10 data; T_a is the effective mean atmospheric temperature; T_{10} is the brightness temperature of Landsat 8 TIRS Band 10; a_{10} and b_{10} are the constants used to approximate the derivative of the Planck radiance function for the TIRS Band 10 given in Table 2; C_{10} and D_{10} are the internal parameters for the algorithm, given as follows:

$$C_{10} = \tau_{10}\varepsilon_{10} \tag{2}$$

$$D_{10} = (I - \tau_{10})[I + (I - \varepsilon_{10})\varepsilon_{10}] \tag{3}$$

where τ_{10} is atmospheric transmittance of Landsat 8 TIRS Band 10 and ε_{10} is the ground emissivity for the band. The improvement was mainly in the determination of the three required parameters (τ_{10}, ε_{10} and T_a) in the mono-window algorithm for LST retrieval from Landsat 8 TIRS Band 10 data, presented in the following sections.

Retrieval of LST from Landsat 8 TIRS data is with the premise that brightness temperature can be computed for the pixels of Band 10 by the mono-window algorithm (Equation (2)). The USGS offers on-demand production of Landsat 8 Operational Land Imager/ Thermal Infrared Sensor (OLI/TIRS) brightness temperature data through EarthExplorer (https://earthexplorer.usgs.gov/).

The upwelling atmospheric radiance is usually estimated by the effective mean atmospheric temperature (T_a) (Sobrino et al., 1991).

$$T_a = 16.0110 + 0.92621T_0 \tag{4}$$

where T_0 (K) is the observed station air temperature at the station elevation. The detail of the mono-window algorithm for LST retrieval from the Landsat 8 data was shown in Wang et al. (2015).

4 Results and Discussion

4.1 Land use and land cover classification

For the validation of the LULC classification, 30 homogeneously covered Landsat pixels were visually extracted for each class from high resolution GF-1A data as validation samples. The overall accuracy was 87.47% and the Kappa coefficient was 0.85 (Table 3). Incorporating inhomogeneous pixels (dominated by more than one class) into the assessment decreased these accuracy indicators.

The classification results showed clearly the distribution and patterns of current land use in the Zhalong wetland (Fig. 2). About 38.53% of the study area was classified as agricultural land. As expected, the dominant agricultural land types were dry farmland (1700 km^2, 35.21% of the Zhalong wetland) and paddy field (160 km^2, 3.32% of the Zhalong wetland). The homogeneity of the agricultural landscape, particularly paddy field, decreased with distance from the river. Wetland covered about 38.49% of the study area. The main wetland types were marsh (1404 km^2, 29.08% of the Zhalong wetland) and water bodies (294 km^2, 6.09% of the Zhalong wetland). During post-classification, errors within the accumulated pixels were eliminated by using settlement polygons provided by the Data Center for Resources and Environmental Sciences, Chinese Academy of Sciences.

Table 2 Determination of coefficients a_{10} and b_{10} for the Landsat 8 TIRS Band 10 (Wang et al., 2015)

Temperature range (℃)	a_{10}	b_{10}	R^2
20–70	−70.1775	0.4581	0.9997
0–50	−62.7182	0.4339	0.9996
−20–30	−55.4276	0.4086	0.9996

Table 3 Confusion matrix for land use and land cover classification measured by land cover classified by Landsat TM in 2006 (%)

	Class	Land cover classified using GF-1A images as ground truth						
		Dry farmland	Paddy field	Marsh	Forest	Saline-alkali land	Resident	Water body
Land cover classified by Landsat NDVI time series	Dry farmland	90.34	0.23	7.93	0.37	0	1.02	0.11
	Paddy field	3.86	95.07	0.83	0.11	0	0.13	0
	Marsh	5.43	0.59	90.91	0.52	1.86	0.09	0.6
	Forest	0.18	0.01	0.07	87.87	0	11.81	0.06
	Saline-alkali land	0	0.51	0	10.55	87.57	1.12	0.25
	Resident	0.19	3.56	0	0	10.57	85.67	0.01
	Water body	0	0.03	0.26	0.58	0	0.16	98.97
	Total	100	100	100	100	100	100	100

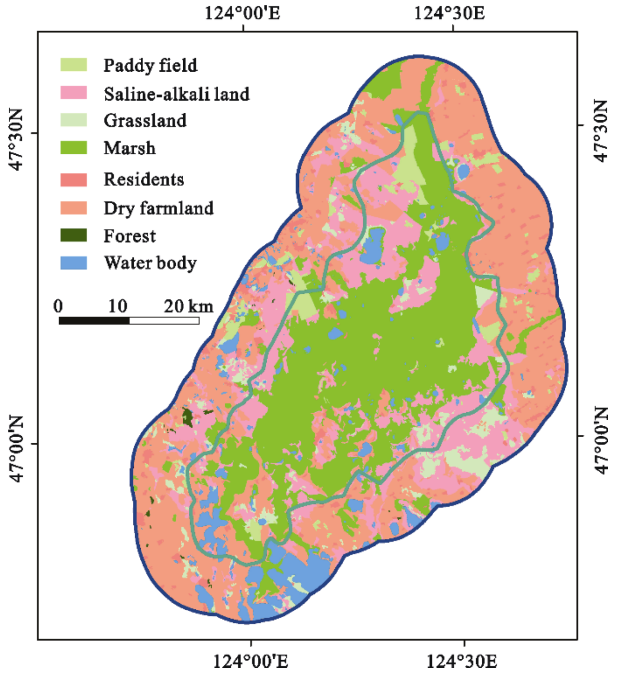

Fig. 2 Spatial distribution of land cover and agricultural land use in the Zhalong wetland in 2017

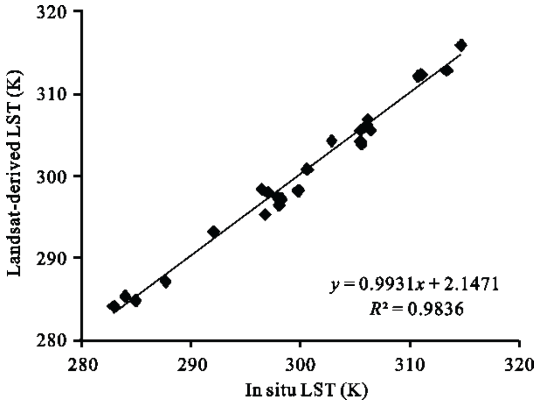

Fig. 3 Comparison between MW inverted LST and ground LST

4.2 Validation of LST

Results for LST estimated from the Landsat 8 TIRS, using the MW algorithm are show in Fig. 3. There is a general underestimation for the four sites except Qiqihaer, as the bias is 0.95 K for this site. The bias for all sites is −1.01 K, suggesting an underestimation for almost all scenes. Absolute errors for Dumeng and Lindian are 1.24 K and 0.82 K, while Fuyu is 1.02 K and average is 1.01 K for all sites (Fig. 3), suggesting that the MW algorithm has the potential for accurate LST inversion from TIRS imagery. Fig. 3 illustrates the comparison of ground and inverted LST, showing that they have a high correlation (R^2 = 0.984). However, there is an underestimation trend in the LST range of 300–310 K. It may result from an error in the estimation of water vapor content, which could also introduce external errors for LST inversion. Meanwhile, the absolute error for the Dumeng site is 1.24 K, higher than other sites. The landscape around Dumeng was checked from the high resolution image in GF-1A and is saline-alkali land and grassland, with several lakes surrounding it. Variations in the landscape lead to emissivity estimation errors, because we only considered soil and vegetation for ε in this study. It may also be noted that the point scale ground measurement does not exactly correspond to the pixel area retrieved from the satellite.

Fig. 4 shows the spatial distribution of the retrieved LST. LST in the region ranged from 274 to 326 K with a mean of 296 K. The wetland's surrounding area has a very high LST, compared with wetland itself. Wetland in the region, especially open water, has the lowest LST due to the strong cooling process resulting from evaporation over the water surface. The LST difference between the surrounding area and the wetland itself may be high, up to ~8 K on the imaging date, as will be seen below.

The LST validation scheme outlined here is anchored to ground based observations. For most mixed vegetated landscapes composed of various land cover types and soils, the LST measured by a station at one specific location (i.e. a point measurement) does not represent the surrounding area that is part of the coarser satellite sensor pixel. For example, different land cover types have associated spatial and temporal variations of surface biophysical parameters, such as vegetation phenology, optical and thermal properties or soil moisture. These all affect the different components of the energy budget. In Guillevic et al. (2012)'s study, a surface energy model was used to estimate these components for a subpixel cell using commonly-measured surface and meteorological parameters. A cell was defined here as an area of homogeneous, or evenly-mixed heterogeneous, vegetation cover. The model was executed for each cell or tile, and then used to estimate the aggregate LST over all subpixel cells. Such a surface energy model would help to validate LST retrieval using meteorological data.

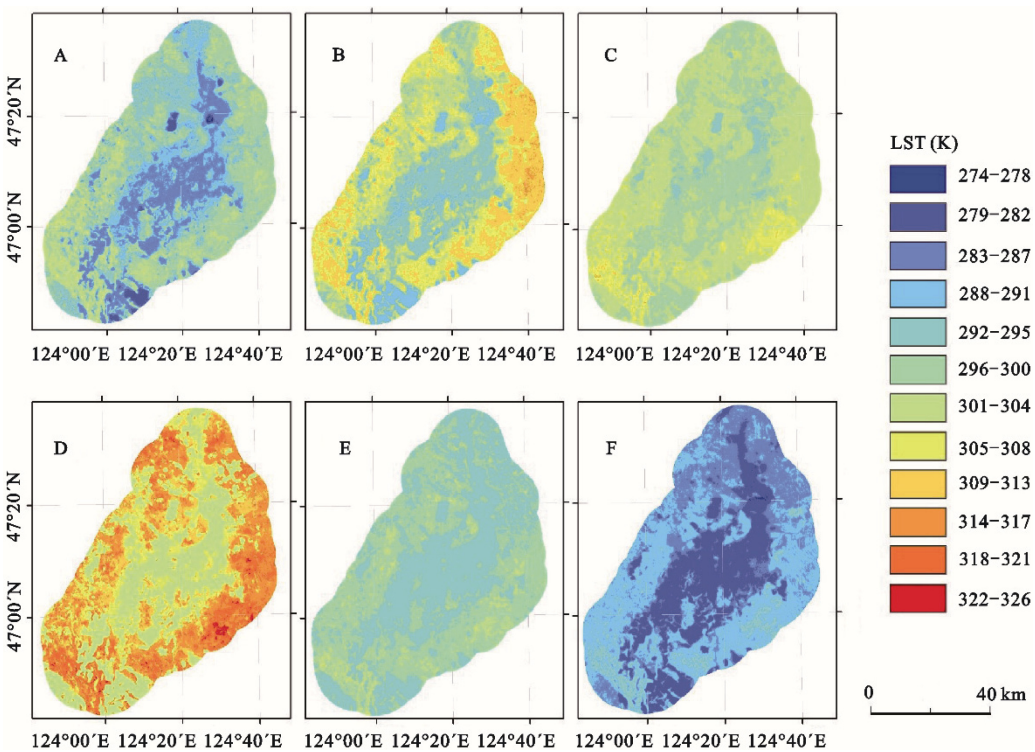

Fig. 4 The LST image retrieved by the mono-window algorithm with Band 10 in Zhalong wetland

4.3 Impact of Zhalong wetland on neighboring LST distribution

To recognize the influence of wetlands on the LST distribution, the mean LST at different buffer distances around Zhalong wetlands has been calculated with the buffer intervals set at 30 m. The static maps (Fig. 5) and the data on Table 4, show that LST is higher with the increasing distance away from the center of wetlands. In general, 500 m is a 'milestone', meaning the influence of wetlands on the LST distribution is obvious when the distance is less than 500 m, but minor when the distance is greater than 500 m. This influence may be due to the following reasons. Wetlands are ecosystems dominated by hydrological processes, which makes their thermodynamics different from other land surfaces. Wetlands have greater thermal capacity and inertia, which decreases the thermal radiation and the exchange intensity between them and their surroundings, influences the surface heat transfer processes and causes local atmospheric circulation. Local thermal abnormalities are ultimately regulated and restrained, which impacts the thermal spatial distribution features and decreases LST around wetlands.

To determine the effect of wetlands on the different LULC LST distributions, the mean LST figures for different LULC of different buffer zones around the Zhalong wetlands have also been calculated, with the buffer interval again set at 30 m. The effect of wetlands on the different LULC LST distributions is shown in in Fig. 5 and Table 4. The distances of influence varied with different surfaces. For saline-alkali land and grassland these distances were 660 and 565 m, while the values for resident, dry farmland and forest were 480, 375 and 405 m respectively. This variation may occur because the vegetation on saline-alkali land and grassland is much shorter than on other surfaces, making aerodynamic resistance lower, thus facilitating heat transfer and evaporation into the air above the canopy. The influence distance for different seasons also varied. Spring, summer and fall were 534, 513 and 444 m, respectively, while the growing season was 497 m. This change may occur because the wind speed in spring is much high than other two seasons, which could magnify heat transfer in the horizontal direction.

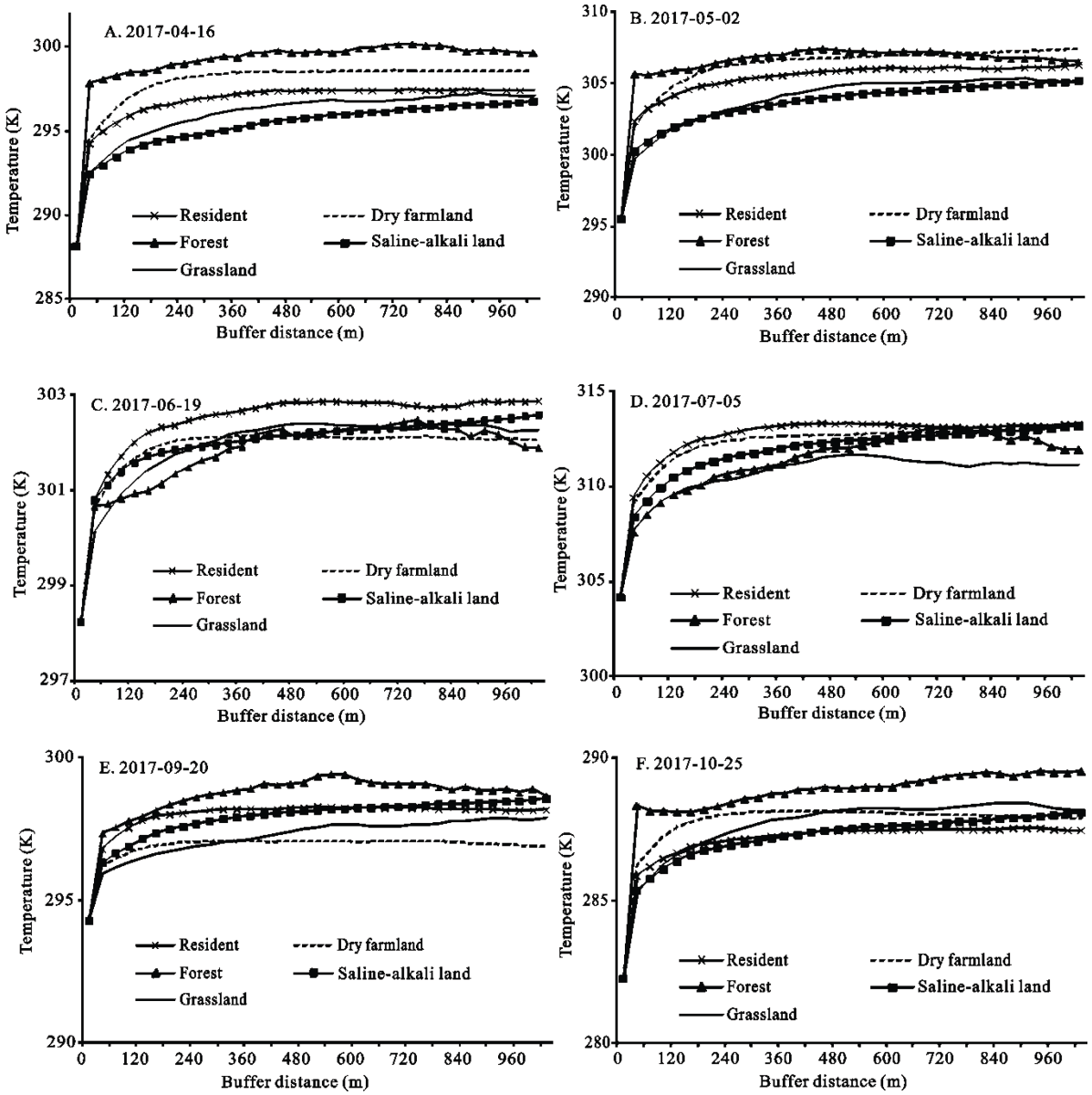

Fig. 5 Land surface temperature of different land uses in the Zhalong wetlands at different buffer radius values

Table 4 Comparison of the wetland cooling effect on different land use/land cover (m)

Date/season	Resident	Dry farmland	Forest	Saline-alkali land	Grassland	Mean value
2017-04-16	450	390	330	750	570	498
2017-05-02	600	450	450	750	600	570
2017-06-19	570	300	450	510	510	468
2017-07-05	450	450	480	870	540	558
2016-09-20	300	300	390	510	570	414
2017-10-25	510	360	330	570	600	474
Spring	525	420	390	750	585	534
Summer	510	375	465	690	525	513
Fall	405	330	360	540	585	444
Growing Season	480	375	405	660	565	497

5 Conclusions

Wetlands play a key role in regulating local climate as well as in reducing the impacts of climate change. Rapid observations of the LST are, therefore, important for understanding wetland systems. With the development of thermal remote sensing technologies, LST retrieval using satellite images is now a practical way to detect the thermal environment of a wetland and its surrounding area from a non-point visual angle rather than traditional detection from a point visual angle. The mono-windows method of retrieving LST has been validated here. On the basis of estimated LST, we used GIS technology to study the impacts of wetland reclamation on local temperatures at a regional scale, after which correlations between LST and wetlands was analyzed.

It is feasible to retrieve the LST from Landsat 8 OLI satellite images with MW model. The model was validated with the land surface temperatures observed at 4 meteorological stations when the satellite scanned the study region, the satellite retrieval error being approximately 1.01°C. The relationship between the spatial distribution of land surface temperatures and the Zhalong wetlands was analyzed based on GIS technology. Results show that LST is higher with increasing distance away from the center of the wetlands. The influence of wetlands on the LST distribution is significant when the distance is less than 500 m, but minor when the distance is more. This phenomenon can be explained by thermodynamic features of wetlands which can influence the surface heat transfer process and cause local atmospheric circulation. Our results also suggest that the influence distance varies for different land cover types. Because the vegetation on saline-alkali land and grassland is much lower than other surfaces, aerodynamic resistance is less, making transfer of heat and water vapor from the evaporating surface into the air above the canopy easier. The influence distance varied according to season as well, perhaps because the wind speed in spring is much faster than other two seasons, an effect which could magnify horizontal heat transfer.

References

Barsi J A, Schott J R, Hook S J et al., 2014. Landsat-8 Thermal Infrared Sensor (TIRS) vicarious radiometric calibration. *Remote Sensing*, 6(11): 11607–11626. doi: 10.3390/rs61111607

Board M E A. Ecosystems and Human Well-Being: Wetlands and Water Synthesis. 2005.

Bonan G B, 1995. Sensitivity of a GCM simulation to inclusion of inland water surfaces. *Journal of Climate*, 8(11): 2691–2704. doi: 10.1175/1520-0442(1995)008<2691:SOAGST>2.0.CO;2

Carlson T N, Capehart W J, Gillies R R, 1995. A new look at the simplified method for remote sensing of daily evapotranspiration. *Remote Sensing of Environment*, 54(2): 161–167.

Carlson T N, Gillies R R, Perry E M, 1994. A method to make use of thermal infrared temperature and NDVI measurements to infer surface soil water content and fractional vegetation cover. *Remote Sensing Reviews*, 9(1–2): 161–173.

Carlson T N, Capehart W J, Gillies R R, 1995. A new look at the simplified method for remote sensing of daily evapotranspiration. *Remote Sensing of Environment*, 54(2): 161–167.

Chen J, Jönsson P, Tamura M et al., 2004. A simple method for reconstructing a high-quality NDVI time-series data set based on the Savitzky-Golay filter. *Remote Sensing of Environment*, 91(3–4): 332–344. doi: 10.1016/j.rse.2004.03.014

Chen Yiyu, 1999. The trends of globle change research in China. *Advance in Earth Sciences*, 14(4): 319–323. (in Chinese)

Chen X L, Zhao H M, Li P X, Yin Z Y, 2006. Remote sensing image-based analysis of the relationship between urban heat island and land use/cover changes. *Remote sensing of environment*, 104(2): 133–146.

Cui Lijuan, 2002. Assessment on Zhalong Wetland value. *Journal of Natural Resources*, 17(4): 451–456. (in Chinese)

Dickinson R E,1991.Global change and terrestrial hydrology-A review. *Tellus*, 43(4): 176–181. doi:10.1034/j.1600-0870.1991.0015.x

Gao Junqin, Lu Xianguo, Li Zhaofu, 2002. Study on cold-humid effect of wetlands in Sanjiang Plain. *Journal of Soil and Water Conservation*, 16(4): 149–151. (in Chinese)

Gao Junqin, Lu Xianguo, Liu Hongyu, 2003. Cold-humid effect of wetlands. *Journal of Ecology and Rural Environment*, 19(1): 18–21. (in Chinese)

Gillespie A, Rokugawa S, Matsunaga T et al., 1998. A temperature and emissivity separation algorithm for Advanced Spaceborne Thermal Emission and Reflection Radiometer (ASTER) images. *IEEE Transactions on Geoscience and Remote Sensing*, 36(4): 1113–1126.

Gong Xiuli, Wang Yiyong, Nie Xiao et al., 2011. Differences in air temperature and relative humidity between a marsh wetland and its surrounding dry farmlands. *Journal of Northeast Forestry University*, 39(11): 93–96, 101. (in Chinese)

Gorham E, 1995. The biogeochemistry of northern peatlands and its possible responses to global warming. In: Woodwell G M and Mackenzie F T (eds). *Biotic Feedbacks in the Global Climate System*. New York: Oxford University Press, 169–187.

Goswami G, Chauhan N, Mal A et al., 2018. Synthesis of 3, 3-Diaryl/Heteroarylpropylamines via Nucleophilic Ring Opening of Activated Azetidines with Arenes and Heteroarenes: New Synthetic Route to (±) Tolterodine. *ACS Omega*, 3(12):

17562–17572.

Guillevic P C, Privette J L, Coudert B et al., 2012. Land surface temperature product validation using NOAA's surface climate observation networks—Scaling methodology for the Visible Infrared Imager Radiometer Suite (VIIRS). *Remote Sensing of Environment*, 124: 282–298. doi: 10.1016/j.rse.2012.05.004

Han M, Sun Y N, Xu S G, 2007. Characteristics and driving factors of marsh changes in Zhalong Wetland of China. *Environmental Monitoring and Assessment*, 127(1–3): 363–381. doi: 10.1007/s10661-006-9286-6

Hostetler S W, 1991. Simulation of lake ice and its effect on the late-Pleistocene evaporation rate of Lake Lahontan. *Climate Dynamics*, 6(1): 43–48. doi: 10.1007/bf00210581

Hostetler S W, Bates G T, Giorgi F, 1993. Interactive coupling of a lake thermal model with a regional climate model. *Journal of Geophysical Research*: *Atmospheres*, 98(D3): 5045–5057. doi: 10.1029/92JD02843

Hu Qiwu, Wu Qin, Liu Ying et al., 2009. A review of carbon cycle in wetlands. *Ecology and Environmental Sciences*, 18(6): 2381–2386. (in Chinese)

Huang Fang, Wang Ping, Wang Yongjie et al., 2007. Ecological environment change and its effect on Siberian White Crane migration in Zhalong Nature Reserve. *Journal of Northeast Normal University* (*Natural Science Edition*), 39(2): 106–111. (in Chinese)

Jiménez-Muñoz J C, Sobrino J A, Skoković D et al., 2014. Land surface temperature retrieval methods from Landsat-8 thermal infrared sensor data. *IEEE Geoscience and Remote Sensing Letters*, 11(10): 1840–1843. doi: 10.1109/lgrs.2014.2312032

Krinner G, 2003. Impact of lakes and wetlands on boreal climate. *Journal of Geophysical Research: Atmospheres*, 108(D16).

Li Feng, Lu Changhu, Yang Hongjun et al., 1998. Community diversity about breeding birds in reed marsh of Zhalong Natural Reserve. *Journal of Northeast Forestry University*, 26(5): 68–72. (in Chinese)

Li Feng, Yang Hongjun, Zhang Honghai et al., 1999. The nest-site selection by red-crowned crane in the Zhalong Wetland. *Journal of Northeast Forestry University*, 27(6): 57–60. (in Chinese)

Li Yintang, Li Zhiyong, Fang Fei et al., 2007. Numerical simulation on cooling and humidifying effects of wetlands. *Journal of Xi'an Jiaotong University*, 41(7): 825–828, 846. (in Chinese)

Lofgren B M, 1997. Simulated effects of idealized Laurentian Great Lakes on regional and large-scale climate. *Journal of Climate*, 10(11): 2847–2858. doi: 10.1175/1520-0442(1997)010<2847:SEOILG>2.0.CO;2

Montanaro M, Gerace A, Lunsford A et al., 2014. Stray light artifacts in imagery from the Landsat 8 Thermal Infrared Sensor. *Remote Sensing*, 6(11): 10435–10456. doi: 10.3390/ rs61110435

Nie Xiao, Wang Yiyong, 2010. 'Cold-humidity island' effect of marsh wetlands on localized micro-climate. *Journal of Ecology and Rural Environment*, 26(2): 189–192. (in Chinese)

Ottlé C, Stoll M, 1993. Effect of atmospheric absorption and surface emissivity on the determination of land surface temperature from infrared satellite data. *International Journal of Remote Sensing*, 14(10): 2025–2037. doi: 10.1080/01431169308954018

Park J, An K, Hwang Y et al., 2004. Ultra-large-scale syntheses of monodisperse nanocrystals. *Nature materials*, 3(12): 891.

Pitman A J, 1991. A simple parameterization of sub-grid scale open water for climate models. *Climate Dynamics*, 6(2): 99–112. doi: 10.1007/bf00209983

Prata A J, 1994. Land surface temperatures derived from the advanced very high resolution radiometer and the along: track scanning radiometer: 2. Experimental results and validation of AVHRR algorithms. *Journal of Geophysical Research: Atmospheres*, 99(D6): 13025–13058.

Price J C, 1983. Estimating surface temperatures from satellite thermal infrared data—A simple formulation for the atmospheric effect. *Remote Sensing of Environment*, 13(4): 353–361. doi: 10.1016/0034-4257(83)90036-6

Qin Z H, Karnieli A, 1999. Progress in the remote sensing of land surface temperature and ground emissivity using NOAA-AVHRR data. *International Journal of Remote Sensing*, 20(12): 2367–2393. doi: 10.1080/014311699212074

Qin Z, Karnieli A, Berliner P, 2001. A mono-window algorithm for retrieving land surface temperature from Landsat TM data and its application to the Israel-Egypt border region. *International Journal of Remote Sensing*, 22(18):3719–3746. doi:10.1080/ 014311600 10006971

Qiu Fuchen, Lin Baoqing, Cai Yongjun et al., 2005. Observation on Siberian white crane migration in spring in Zhalong Nature Reserve. *Journal of Northeast Forestry University*, 33(1): 103–105. (in Chinese)

Rozenstein O, Qin Z H, Derimian Y et al., 2014. Derivation of land surface temperature for Landsat-8 TIRS using a split window algorithm. *Sensors*, 14(4): 5768–5780. doi: 10.3390/s140405768

Saaroni H, Ziv B, 2003. The impact of a small lake on heat stress in a Mediterranean urban park: the case of Tel Aviv, Israel. *International Journal of Biometeorology*, 47(3): 156–165. doi: 10.1007/s00484-003-0161-7

Savitzky A, Golay M J, 1964. Smoothing and differentiation of data by simplified least squares procedures. *Analytical chemistry*, 36(8): 1627–1639.

Sobrino J A, Coll C, Caselles V, 1991. Atmospheric correction for land surface temperature using NOAA-11 AVHRR channels 4 and 5. *Remote Sensing of Environment*, 38(1): 19–34. doi: 10.1016/0034-4257(91)90069-I

Song Changchun, 2003. Advance in research on carbon cycling in wetlands. *Scientia Geographica Sinica*, 23(5): 622–628. (in Chinese)

Tong Chuan, Zeng Congsheng, 2006. Review and analysis on carbon cycling and carbon balance model in wetlands ecosystem. *Journal of Subtropical Resources and Environment*, 1(3): 84–92. (in Chinese)

Tong Shouzheng, Lu Xianguo, Su Liying et al., 2008. Changing process and the impact factors of wetland ecosystem in Zha-

long Wetland. *Wetland Science*, 6(2): 179–184. (in Chinese)

United States Geological Survey, 2014. Landsat 8 Operational Land Imager and Thermal Infrared Sensor calibration notices. http://landsat.usgs.gov/calibration_notices.php

Wang F, Qin Z H, Song C Y et al., 2015. An improved mono-window algorithm for land surface temperature retrieval from Landsat 8 thermal infrared sensor data. *Remote Sensing*, 7(4): 4268–4289. doi: 10.3390/rs70404268

Wand Hao, Xu Shiguo, Sun Leshi, 2006. Effects of climatic change on evapotranspiration in Zhalong wetland, Northeast china. *Chinese Geographical Science*, 16(3): 265–269. doi: 10.1007/s11769-006-0265-1

Wang Yongjie, Luo Jinming, Ye Yajie et al., 2009. Influence on Zhalong Wetland succession by seasonal frozen–thawing action. *Journal of Soil and Water Conservation*, 23(5): 34–38, 43. (in Chinese)

Wo Xiaotang, Sun Yankun, 2010. Study on dynamic change of land use and land cover in Zhalong Wetland. *Journal of Northeast Agricultural University*, 41(1): 56–60. (in Chinese)

Yang Ping, Tong Chuan, 2011. Effects of LUCC on carbon stocks and emission in wetland. *Wetland Science & Management*, 7(3): 56–59. (in Chinese)

Yuan Li, Gong Wenfeng, Yu Chenglong, 2009. Spatial-temporal changes of habitats for red-crowned cranes in Zhalong Wetland based on RS and GIS. *Journal of Northeast Forestry University*, 37(8): 34–38. (in Chinese)